

## Article

# Effect of Iron-Doping on the Structure and Photocatalytic Activity of TiO<sub>2</sub> Nanoparticles

Cátia Afonso <sup>1,\*</sup>, Orlando Lima, Jr. <sup>2</sup>, Iran Rocha Segundo <sup>1,2,\*</sup>, Salmon Landi, Jr. <sup>3</sup>, Élide Margalho <sup>2</sup>, Natália Homem <sup>4</sup>, Mário Pereira <sup>1</sup>, Manuel F. M. Costa <sup>5</sup>, Elisabete Freitas <sup>2</sup> and Joaquim Carneiro <sup>1,\*</sup>

<sup>1</sup> Centre of Physics of Minho and Porto Universities (CF-UM-UP), Azurém Campus, University of Minho, 4800-058 Guimarães, Portugal

<sup>2</sup> ISISE, Department of Civil Engineering, Azurém Campus, University of Minho, 4800-058 Guimarães, Portugal

<sup>3</sup> Federal Institute Goiano, Rio Verde 75901-970, GO, Brazil

<sup>4</sup> Digital Transformation CoLab (DTx), Building 1, Campus of Azurém, University of Minho, 4800-058 Guimarães, Portugal

<sup>5</sup> Centre of Physics of Minho and Porto Universities (CF-UM-UP), Gualtar Campus, University of Minho, 4710-057 Braga, Portugal

\* Correspondence: catiaj\_afonso@hotmail.com (C.A.); iran@civil.uminho.pt (I.R.S.); carneiro@fisica.uminho.pt (J.C.)

**Abstract:** This research reports a simple, innovative, and low-cost doping method of TiO<sub>2</sub> nanoparticles presenting the effects of calcination and the weight ratio of TiO<sub>2</sub>:FeCl<sub>3</sub> (1:0.33–1:4.5). The photocatalytic activity of the nanomaterials was investigated by decolorizing Rhodamine B (RhB) dye in an aqueous solution. The main results showed that there is anatase-to-rutile transformation after the calcination process. The Fe-doped process modified the TiO<sub>2</sub> spectrum and showed a connection in the Ti–O–Fe vibration. The particle size is within the nanometer range, between 20–51 nm, except for calcined TiO<sub>2</sub>. The inclusion of Fe in TiO<sub>2</sub> decreased the band gap energy from 3.16 (reference) up to 2.06 eV (1:3). Additionally, after the calcination, there was a decrease in this value from 3.03 eV (reference) up to 1.95 eV (1:1.6). The TiO<sub>2</sub>, with a ratio of (1:1.6), showed the highest activity in the photocatalytic degradation of RhB with an efficiency of 93.8% after 3 h of irradiation.



**Citation:** Afonso, C.; Lima, O., Jr.; Segundo, I.R.; Landi, S., Jr.; Margalho, É.; Homem, N.; Pereira, M.; Costa, M.F.M.; Freitas, E.; Carneiro, J. Effect of Iron-Doping on the Structure and Photocatalytic Activity of TiO<sub>2</sub> Nanoparticles. *Catalysts* **2023**, *13*, 58. <https://doi.org/10.3390/catal13010058>

Academic Editors: Magdalena Janus and Kangle Lv

Received: 30 October 2022

Revised: 22 December 2022

Accepted: 23 December 2022

Published: 27 December 2022



**Copyright:** © 2022 by the authors. Licensee MDPI, Basel, Switzerland. This article is an open access article distributed under the terms and conditions of the Creative Commons Attribution (CC BY) license (<https://creativecommons.org/licenses/by/4.0/>).

**Keywords:** semiconductor; band gap energy; diffuse reflectance; co-precipitation method

## 1. Introduction

Titanium dioxide (TiO<sub>2</sub>) is a widely studied semiconductor because of its optical and electronic properties, good chemical stability, availability, and low-cost [1–7]. These characteristics cause TiO<sub>2</sub> to be one of the most promising photocatalysts for treating various environmental pollutants. In large-scale and practical applications, the use limitations of TiO<sub>2</sub> as a material for the photocatalytic process [5] are mainly 3: TiO<sub>2</sub> absorbs only a small part of sunlight in the visible region, making photocatalytic activity at wavelengths less than 400 nm [5,8], the low quantum yield is due to the easy matching of photogenerated electron pairs, and its band gap energy (E<sub>g</sub>) range of 3.0–3.2 eV, which is quite large [9–11].

TiO<sub>2</sub> is an extrinsic n-type semiconductor in three crystallographic structures: anatase, rutile, and brookite. The anatase and rutile phases are the most frequently used in photocatalytic processes. The low recombination rate of its photogenerated electrons and holes on the TiO<sub>2</sub> surface causes the anatase phase to show better photoactivity [12–14].

An acceleration of the chemical reaction is required to occur photocatalysis. Their shortened band gap energy and distinct electronic structure cause semiconductor materials such as TiO<sub>2</sub>, ZnO, CeO<sub>2</sub>, CdS, ZnS, Fe<sub>2</sub>O<sub>3</sub>, and others to be chosen as photocatalysts. When these semiconductors are stimulated by solar irradiation, energy levels higher than their band gap energy must be reached [6,15].

Doping in TiO<sub>2</sub> nanoparticles changes the electronic structure of TiO<sub>2</sub> by modifying their chemical composition and optical properties [16]. To decrease the band gap

energy down to wavelengths of visible light, doping with metal ions, such as iron, nickel, chromium, zinc, platinum, and manganese, among others, has been studied. Research aimed at decreasing the recombination rate of the  $e^-/h^+$  pair and thus increasing the yield of the photocatalytic process by modifying the semiconductor surfaces with the addition of metal ions [5,9,14,16–22]. Doping with metal ions increases the recombination time of the  $e^-/h^+$  pair making the holes accessible for forming  $\bullet\text{OH}$  radicals [15].

Sunlight comprises visible and infrared photons, with only 3–5% of the ultraviolet (UV) range. More research is underway on doping  $\text{TiO}_2$  nanoparticles to increase photocatalytic efficiency [4–6,23,24] which will explain how the physical and chemical properties of  $\text{TiO}_2$  determine the photocatalytic activity and develop affordable and appropriate synthesis methods to obtain  $\text{TiO}_2$  with superior photocatalytic efficiency [5,14,17,25].

The inclusion of iron ( $\text{Fe}^{3+}$ ) allows a broad absorption of the solar spectrum in the visible region. Consequently, the potential for photocatalytic activity is increased since the radius of  $\text{Fe}^{3+}$  (0.64 Å) and  $\text{Ti}^{4+}$  (0.68 Å) are very close in terms of size [8,16,26]. Thus, doped- $\text{TiO}_2$  is essential for outdoor applications to maximize photocatalytic efficiency [4,27,28]. For synthesizing Fe-doped  $\text{TiO}_2$ , different methods are currently used, such as sol-gel [29,30], ultrasonic radiation-assisted hydrothermal [31], molten salt [6], wet-chemical synthesis [32], and co-precipitation [18], among others. For example, Ghorbanpour et al. (2019) synthesized and characterized Fe-doped  $\text{TiO}_2$  nanoparticles prepared by the molten salt method and calcination process. The band gap energy of the Fe-doped  $\text{TiO}_2$  samples decreased with increasing Fe concentration from 3.1 eV for pure  $\text{TiO}_2$  to 3.02–2.80 eV for Fe-doped  $\text{TiO}_2$ . Thus, the photocatalytic activity was higher for the Fe-doping content of 0.5 wt.% than for pure  $\text{TiO}_2$  [6]. Another process was addressed by Carneiro et al. (2014), who investigated the incorporation of Fe into  $\text{TiO}_2$  nanoparticles through a ball milling process using stainless steel balls. They concluded that there are improvements in photocatalytic activity (over 60% at about 120 min) and higher rotational speeds [5].

Moreover, Ganesh et al. (2012) studied different amounts of Fe-doped  $\text{TiO}_2$  by the co-precipitation method. They found that small amounts of Fe (0.1 wt.%) are sufficient to transform  $\text{TiO}_2$  from the rutile phase to the full anatase phase and achieve higher photocatalytic activity [18]. From another approach, Adamek et al. (2012) compared the results of photocatalytic degradation with the presence of  $\text{TiO}_2$  or Fe (III) salts as well as a mixture of  $\text{TiO}_2$  with Fe (III), more properly with  $\text{FeCl}_3$ . They concluded that the photodegradation rate constant ( $k$ ) of  $\text{TiO}_2/\text{FeCl}_3$  (pH = 3) is approximately four times the rate of the undoped  $\text{TiO}_2$ . Consequently, adding  $\text{FeCl}_3$  to  $\text{TiO}_2$  nanoparticles significantly increases the photocatalytic activity by UVA irradiation in the 400–320 nm range after 120 min of stirring [8].

This paper investigated the process of  $\text{TiO}_2$  doping with different concentrations of iron chloride ( $\text{FeCl}_3$ ) via the co-precipitation method. This study is relevant as it aims to improve on and innovate the photocatalysis processes since different percentages of  $\text{FeCl}_3$  in  $\text{TiO}_2$  are studied using a simple method. Additionally, this method is low-cost in terms of doped  $\text{TiO}_2$  production that will be used as an efficient photocatalyst when activated under UV radiation and visible light, and will therefore be used to, for example, capture pollutants. Hereafter, the optical, structural, chemical, morphological, and photocatalytic properties of Fe-doped  $\text{TiO}_2$  are presented and explored before and after calcination.

## 2. Results and Discussion

### 2.1. Fourier-Transform Infrared Spectroscopy (FTIR)

The FTIR spectra of the undoped  $\text{TiO}_2$  (reference),  $\text{FeCl}_3$  (reference), and  $\text{TiO}_2$  doped with various concentrations of  $\text{FeCl}_3$  before and after the calcination process are shown in Figure 1. The H–O–H vibrational bonds are related to the peaks at 3803, 3382, and 3439  $\text{cm}^{-1}$ , and the  $\text{H}_2\text{O}$  vibrational bonds are indexed to the peaks at 1626  $\text{cm}^{-1}$  [33]. These indicate the presence of absorbed hydroxyl groups in the samples [34]. In the photocatalytic process, all oxygen-containing groups play an influential role in the photocatalytic activity and are also capable of generating more hydroxyl radicals [35]. The Ti–O–Fe vibration is

present at the peak of  $2285\text{ cm}^{-1}$ , which is a bond from the doping process [36]. The peaks observed in the range  $932\text{--}826\text{ cm}^{-1}$  are due to the Ti–O group [37].

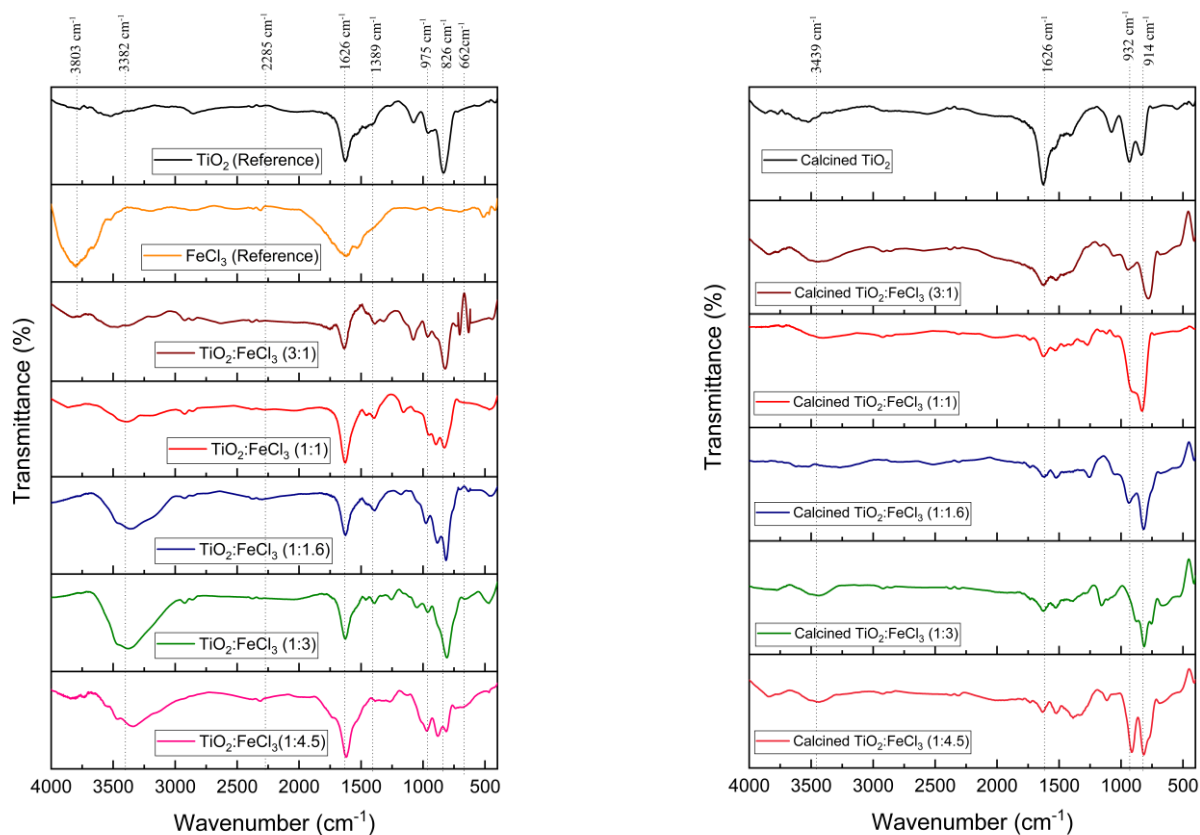


**Figure 1.** FTIR spectra for the  $\text{TiO}_2$  (reference),  $\text{FeCl}_3$  (reference), and the samples synthesized before calcination (left) and after calcination (right).

Concerning the  $\text{TiO}_2$  reference spectrum, the Ti–O–Ti bond and the Ti–O stretching vibration correspond to the  $800\text{--}1200\text{ cm}^{-1}$  peaks. Regarding the Fe-doped  $\text{TiO}_2$  peaks, the O–Ti–O vibration and the Fe–O–Fe symmetric stretching vibration are at  $1389\text{ cm}^{-1}$ . The peak observed at  $662\text{ cm}^{-1}$  proves the existence of iron oxyhydroxide Fe–O–OH. The similarity between the peak values of the chemical bonds below  $1000\text{ cm}^{-1}$  means that the Fe–O and Ti–O bending frequency overlap may occur.

Thus, for the different  $\text{TiO}_2\text{:FeCl}_3$  ratios, there are no significant differences in the material chemical bonds either before or after the calcination process. Nevertheless, the Ti–O–Fe vibration and the hydroxyl groups decrease with the calcination process.

## 2.2. X-ray Diffraction (XRD)

Figure 2 shows the XRD patterns of the doped  $\text{TiO}_2$  nanoparticles before and after calcination. For each of the samples synthesized, there are no significant differences between the XRD patterns and  $\text{TiO}_2$  nanoparticles (reference). This means that the fraction of the anatase phase in the doped  $\text{TiO}_2$  nanoparticles has the same magnitude as  $\text{TiO}_2$  (reference). Therefore, the doping process has no relevant influence on anatase-to-rutile transformation (ART), but after calcination, there is an ART.

It is generally observed that the diffraction peaks become slightly broader after the calcination of Fe-doped  $\text{TiO}_2$ . Their relative intensities decrease for the anatase phase and increase for the rutile phase. The XRD spectrum peaks of the anatase phase, crystal planes (101), (105), and (200), and the diffraction planes (110) and (101) of the rutile phase were chosen to determine the average crystallite size, lattice parameters and weight fraction of anatase phase in the doped and calcined powders.

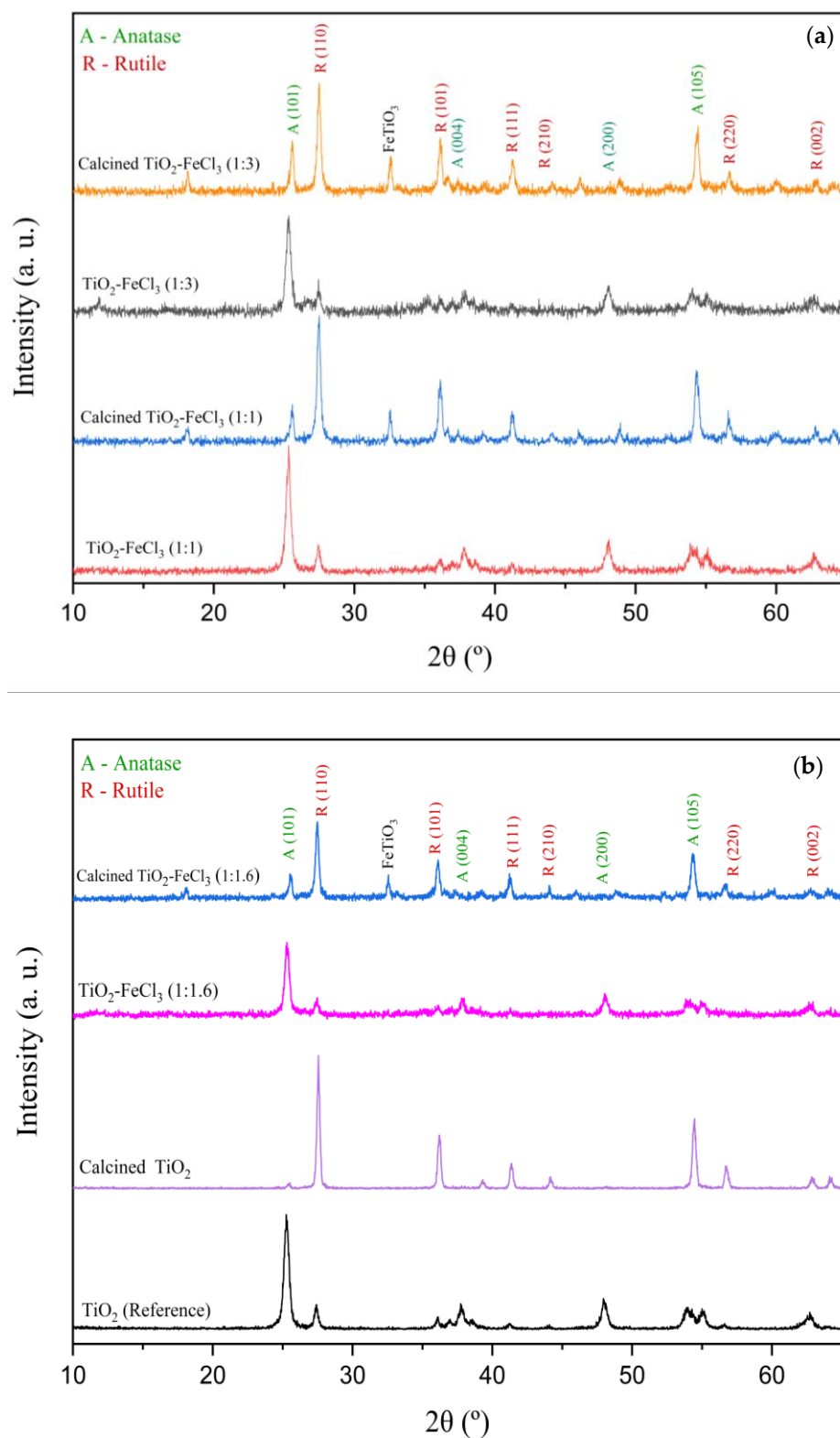


**Figure 2.** X-ray diffraction patterns of doped and undoped  $\text{TiO}_2$  before and after calcination: (a) 1:3 and 1:1 and (b) 1:1.6 and reference.

After the calcination process, the new peak in the XRD spectrum at  $2\theta = 32.56^{\circ}$  refers to  $\text{FeTiO}_3$  (ilmenite). The intensity of this peak is the same for the increasing concentration of  $\text{FeCl}_3$  in  $\text{TiO}_2$ , as observed by Ganesh et al. (2007). These researchers prepared Fe-doped  $\text{TiO}_2$  powders by the co-precipitation method and cited the appearance of small

amounts of secondary phases  $\alpha$ -Fe<sub>2</sub>O<sub>3</sub> and FeTiO<sub>3</sub> in their doped samples [18]. In the present study, only FeTiO<sub>3</sub> appeared in the calcination process after TiO<sub>2</sub> doping. On the contrary, Ghorbanpour et al. (2019) studied iron-doped TiO<sub>2</sub> at various concentrations with a calcination process. They reported that no iron-related peaks appeared, i.e., there was no solid iron-titanium solution [6]. The reason for this behavior and the appearance of these new peaks are yet to be fully understood.

As shown in Table 1, before the calcination process, relative to the anatase phase, the crystallite size of TiO<sub>2</sub> (reference) nanoparticles is about 18.49 nm. The Fe-doped TiO<sub>2</sub> nanoparticles' sizes were 19.40 nm, 19.85 nm, and 19.68 nm, i.e., for the ratios of TiO<sub>2</sub>-FeCl<sub>3</sub> at (1:1), (1:1.6), and (1:3), respectively. For the rutile phase, the crystallite size of TiO<sub>2</sub> nanoparticles (reference) is about 29.75 nm. The increasing Fe-doped concentration ranges from 22.05 nm to 25.74 nm, respectively. After the calcination process, the crystallite size of the calcined TiO<sub>2</sub> nanoparticles was about 18.53 nm, i.e., there was no significant difference between the TiO<sub>2</sub> (reference) and the calcined TiO<sub>2</sub>.

**Table 1.** Influence of doped material before and after calcination as to the on average crystallite size, lattice parameters, unit cell volume, and anatase phase fraction for doped TiO<sub>2</sub> nanoparticles.

Composition	Crystallite Size (nm)		Lattice Parameters (Å)				Unit Cell Volume (Å <sup>3</sup> )		XA (%)
	Anatase	Rutile	Anatase		Rutile		Anatase	Rutile	
			a	c	a	c			
TiO <sub>2</sub> (reference)	18.4879	29.7536	3.7907	9.5154	4.5946	2.9613	136.7307	62.5141	80.82
Calcined TiO <sub>2</sub>	18.5277	32.2752	3.7531	9.4134	4.5717	2.9288	132.5949	61.2132	37.31
TiO <sub>2</sub> -FeCl <sub>3</sub> (1:1)	19.4046	22.0470	3.7832	9.4710	4.5913	2.9605	135.5547	62.4074	87.95
Calcined TiO <sub>2</sub> -FeCl <sub>3</sub> (1:1)	28.1559	26.3592	3.7523	9.4259	4.5814	2.9558	132.7144	62.0399	37.16
TiO <sub>2</sub> -FeCl <sub>3</sub> (1:1.6)	19.8477	22.6825	3.7833	9.7596	4.5847	2.9595	139.6927	62.2071	92.90
Calcined TiO <sub>2</sub> -FeCl <sub>3</sub> (1:1.6)	28.8106	27.4820	3.7447	9.4408	4.5864	2.9557	132.3862	62.1733	42.30
TiO <sub>2</sub> -FeCl <sub>3</sub> (1:3)	19.6765	25.7432	3.7855	9.3839	4.5913	2.9644	132.5812	62.4897	60.27
Calcined TiO <sub>2</sub> -FeCl <sub>3</sub> (1:3)	29.9340	27.0145	3.7424	9.4242	4.5814	2.9558	131.9912	62.0399	41.69

With the addition of Fe-doped, the crystallite size increased with increasing concentration, from 19.40 nm to 29.93 nm. Thus, for the anatase phase, there is a significant difference between the crystallite size for the doped material with the material after calcination. However, for the rutile phase, crystallite size increases compared to the doped material with the calcined one. In the rutile phase, the TiO<sub>2</sub> doped nanoparticles after the calcination process were about 32.28 nm. With the increase of FeCl<sub>3</sub> concentration, the crystallite size changed between 26.36 nm to 27.02 nm. Compared to the calcined TiO<sub>2</sub>, the crystallite size is smaller. Thus, there was an anatase-to-rutile transformation (ART) for the calcination process. Since the ionic radii of titanium and iron are close (Ti<sup>4+</sup> (0.68 Å) and Fe<sup>3+</sup> (0.64 Å)), the incorporation of the iron ion into the crystal structure of TiO<sub>2</sub> in the anatase phase may occur [6,18].

The lattice parameters were calculated and compared with the crystallographic data of reference TiO<sub>2</sub> collected from the JCPDS International Tables for Crystallographers No. 21-1272 for the anatase phase and No. 21-1276 for the rutile phase. Thus, for the anatase phase, parameter a is 3.7852 Å, and parameter c is 9.5139 Å; for the rutile phase, the parameter a is 4.5933 Å, and the parameter c is 2.9592 Å.

For the set of samples studied, doped and after calcination, the values obtained for parameter a in the anatase phase range from 3.7424 Å to 3.7907 Å, and for the lattice parameter c, range from 9.3839 Å to 9.7596 Å. These parameters differ slightly from the theoretical values. The lattice parameter a ranges from a maximum decrease of 1.13% to an increase of 0.15%. The lattice parameter c ranges from a maximum decrease of 1.37% to a maximum increase of 2.58%. Regarding the rutile phase, parameter a ranges from 4.5717 Å to 4.5946 Å, and parameter c from 2.9288 Å to 2.9644 Å. Similarly, the lattice parameter a range from a maximum decrease of 0.47% to a maximum increase of 0.03%. The parameter c ranges from a maximum reduction of 1.03% to a maximum increase of 0.07%. This may refer to the displacement of atoms from their ideal locations [38]. For each sample, there is

no significant difference in the lattice parameters, anatase and rutile phases, and unit cell volume ( $\text{\AA}^3$ ).

Finally, regarding the fraction of the anatase phase before the calcination process,  $\text{TiO}_2$  (reference) showed a fraction of 80.82%. In the Fe-doped synthesized samples, the ratios (1:1), (1:1.16), and (1:3) showed a fraction of 87.95%, 92.90%, and 60.27%, respectively. After the calcination process, there is a marked decrease in calcined  $\text{TiO}_2$  (37.31%), compared to  $\text{TiO}_2$  (reference), and for the different ratios of (1:1), (1.16) and, i.e., 37.16%, 42.30%, and 41.69%.

Before the calcination process, the different  $\text{TiO}_2:\text{FeCl}_3$  ratios show similar behavior for the crystallite size in the anatase phase and a slight difference for the rutile phase. Additionally, they show no significant differences in the lattice parameters and unit cell volume compared to  $\text{TiO}_2$  (reference). After the calcination process, the different ratios  $\text{TiO}_2:\text{FeCl}_3$  show an increase in crystallite size, a decrease in unit cell volume, and a sharp decrease for the anatase phase fraction, with  $X_A$  of about 37–41%.

### 2.3. Scanning Electron Microscopy (SEM) and Energy Dispersive Spectroscopy (EDS)

SEM was employed to investigate the homogenization and dispersion of the samples. EDS was performed to analyze their chemical characterization, i.e., elemental analysis of each material. For the analysis, the following samples were selected: (a)  $\text{TiO}_2$  (reference), (b) calcined  $\text{TiO}_2$ , and in the different ratios of  $\text{TiO}_2:\text{FeCl}_3$  doped (c) (1.16), (d) calcined (1:1.6), and (e) (1:3). Figure 3 presents the SEM microscopy representations and the EDS spectrum.

For the reference  $\text{TiO}_2$  (Figure 3a) it is possible to verify the nanometer scale size nanoparticles of  $\text{TiO}_2$ , ranging from 20 to 30 nanometers; for the reference  $\text{TiO}_2$ , after the calcination process, the size of the particles is approximately 50 nm (Figure 3b), indicating that the particles have practically doubled their diameter. Additionally, the surface of the particles became smoother and more regular before the calcination process.

Concerning the  $\text{TiO}_2$  doped with  $\text{FeCl}_3$  at the ratio of (1:1.6), it can be inferred that iron is present in the sample, and the positions of the spectrum's peaks confirm it. Furthermore, the particle size remains similar to the reference  $\text{TiO}_2$  (Figure 3c). Since the different particles of  $\text{TiO}_2$  and Fe cannot be observed separately, there are indications of a chemical reaction between them in the doping process; they become single particles, as indicated. Iron is not distributed heterogeneously into the  $\text{TiO}_2$  nanoparticles. It is also noticed that there are Cl residues in the spectrum of this sample. After the calcination process (Figure 3d) the same magnitude of particle size follows as the calcined  $\text{TiO}_2$ . A change in surface appearance to smoother and more regular than before the calcination process was observed. The disappearance of residual Cl occurred, which may be caused by the washing step of the doping process.

Finally, the (1:3) ratio of Fe-doped  $\text{TiO}_2$  was analyzed before the calcination process (Figure 3e). It can be observed that the particle dimensions remain with the same size magnitude as the non-calcined reference  $\text{TiO}_2$  particles, and there is a residual amount of Cl remaining from the washing step of the doping process. In this case, there are also indications of the chemical reaction between  $\text{TiO}_2$  and Fe.

To summarize the results, Table 2 presents each sample's chemical composition and particle size. The particle sizes show some variation, as observed in the XRD. The  $\text{TiO}_2$  (reference) has a particle size between 20–30 nm and is composed of 65.49% titanium and 34.51% oxygen. With respect to calcined  $\text{TiO}_2$ , the size increases, i.e., ranging between 50–108 nm, but the chemical composition is similar to  $\text{TiO}_2$  (reference). Regarding the different  $\text{TiO}_2:\text{FeCl}_3$  ratios, the particle size varies between 23–27 nm, and 27–38 nm, for ratios (1:1.16) and (1:3), respectively. After the calcination process at the ratio (1:1.6), the size also increased (49–51 nm). In the different proportions, there is the appearance of iron (Fe) with 14.00 to 17.95% and chlorine (Cl) with 1.85 to 2.48%. In the proportion (1:1.6) after the calcination process, chlorine is no longer present in the chemical composition.

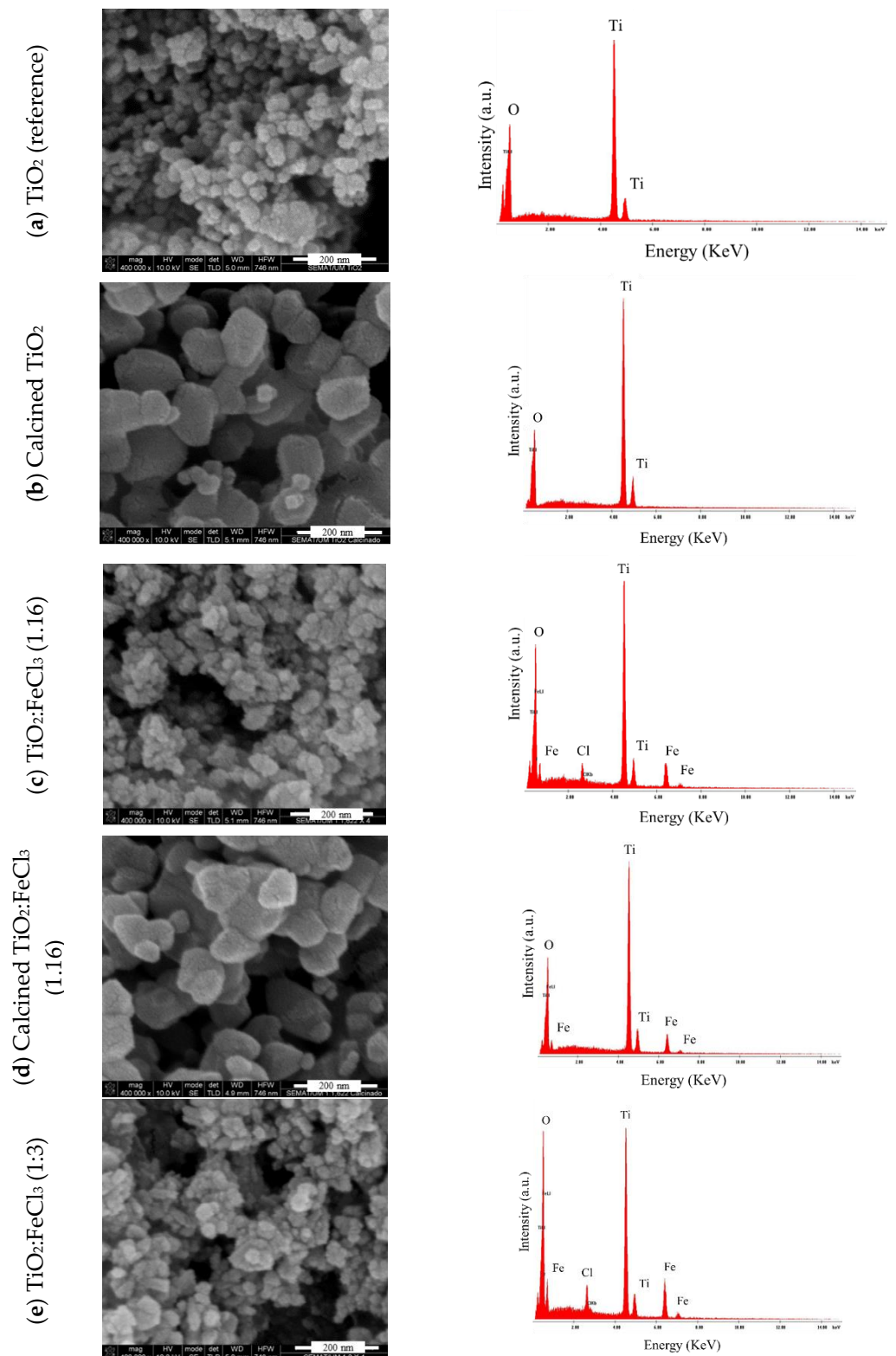


**Figure 3.** SEM micrograph representation (left) and EDS spectrum (right) of: (a) reference  $\text{TiO}_2$ , (b) calcined  $\text{TiO}_2$ , (c)  $\text{TiO}_2\text{-FeCl}_3$  (1:1.6), (d) calcined  $\text{TiO}_2\text{-FeCl}_3$  (1:1.6) and (e)  $\text{TiO}_2\text{-FeCl}_3$  (1:3).

Thus, before the calcination process, all  $\text{TiO}_2:\text{FeCl}_3$  ratios show a similar particle size. After the calcination process, an increase in particle size occurs that is caused by the anatase-to-rutile transformation (ART), as previously discussed in XRD test results section.

**Table 2.** Particle size variation and characterization of each sample studied.

Samples	Particle Size (nm)	Chemical Composition (%)			
		Ti *	O *	Fe *	Cl *
TiO <sub>2</sub> (reference)	20–30	65.49	34.51	-	-
Calcined TiO <sub>2</sub>	50–108	66.79	33.21	-	-
TiO <sub>2</sub> -FeCl <sub>3</sub> (1:1.6)	23–27	44.98	39.14	14.02	1.85
Calcined TiO <sub>2</sub> -FeCl <sub>3</sub> (1:1.6)	49–51	50.69	35.31	14.00	-
TiO <sub>2</sub> -FeCl <sub>3</sub> (1:3)	27–38	37.80	41.77	17.95	2.48

\* Ti: Titanium; O: Oxygen; Fe: Iron; Cl: Chlorine.

#### 2.4. Diffuse Reflectance Spectroscopy (DRS)

To study the effectiveness of TiO<sub>2</sub> doping with FeCl<sub>3</sub>, the band gap of the semiconductor nanoparticles was analyzed using diffuse reflectance spectroscopy (DRS) and the Kubelka–Munk transform. The measurement of the light absorption of each material doped with different concentrations of FeCl<sub>3</sub> and TiO<sub>2</sub> (reference) before and after the calcination process (Figure 4) was obtained using the Kubelka–Munk function. The results show that both materials, calcined or uncalcined reference TiO<sub>2</sub>, depicts strong photoabsorption at wavelengths below 400 nm, i.e., in the ultraviolet (UV) and visible regions. For all concentrations, before and after calcination, the doped TiO<sub>2</sub> shows a shift of the absorption edge that is caused by the effect of iron (i.e., dashed curves). However, as intended, changes in the optical properties of the material occur in the process of doping with Fe.

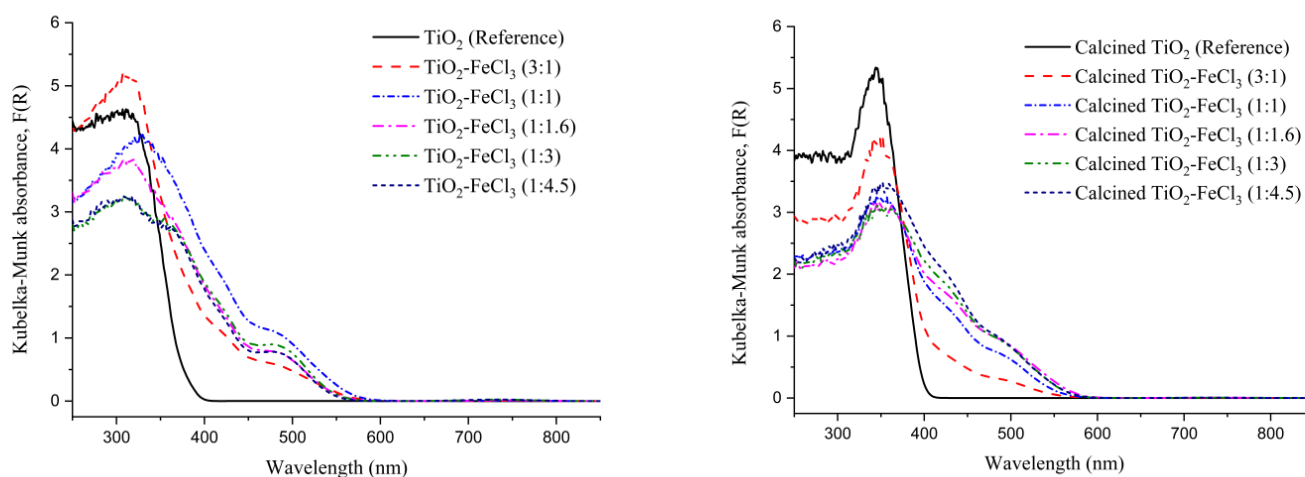


**Figure 4.** Kubelka–Munk function versus wavelength for the undoped TiO<sub>2</sub> (reference) and the samples synthesized before calcination (**left**) and after calcination (**right**).

These shifts of the absorption edge to a longer wavelength indicate the band gap energy ( $E_g$ ) of TiO<sub>2</sub> and an increase of the absorption into the visible light region, which is less energetic than the UV region. The values of the Kubelka–Munk transformation versus Energy (eV) can be seen in Figure 5. A tangent line to the inflection point was drawn on the curve to obtain the value of  $E_g$ .

It can be observed that the  $E_g$  values for the undoped TiO<sub>2</sub> (reference) non-calcined (3.16 eV) and calcined (3.03 eV) are higher if compared to the doped TiO<sub>2</sub> with FeCl<sub>3</sub> in different concentrations. For both calcined or not calcined situations, the  $E_g$  values were always the lowest for the concentrations (1:1), (1:1.6), and (1:3). After the calcination process, the  $E_g$  values tend to decrease, except for the situation (3:1). Before calcination, the concentrations (1:1), (1:1.6), and (1:3) presented  $E_g$  values of 2.08, 2.21, and 2.06 eV, respectively. After calcination, the  $E_g$  of these situations became 2.10, 2.11, and 2.03 eV, respectively. After the calcination process, there is a strong tendency for  $E_g$  to decrease, which may be related to the ART, i.e.,  $E_g$  (rutile) <  $E_g$  (anatase), to the formation of a dopant

energy level ( $\text{Fe}^{4+}/\text{Fe}^{3+}$ ), which comes in the excitation of  $\text{Fe}^{3+}$  and also due to the increase in particle size.

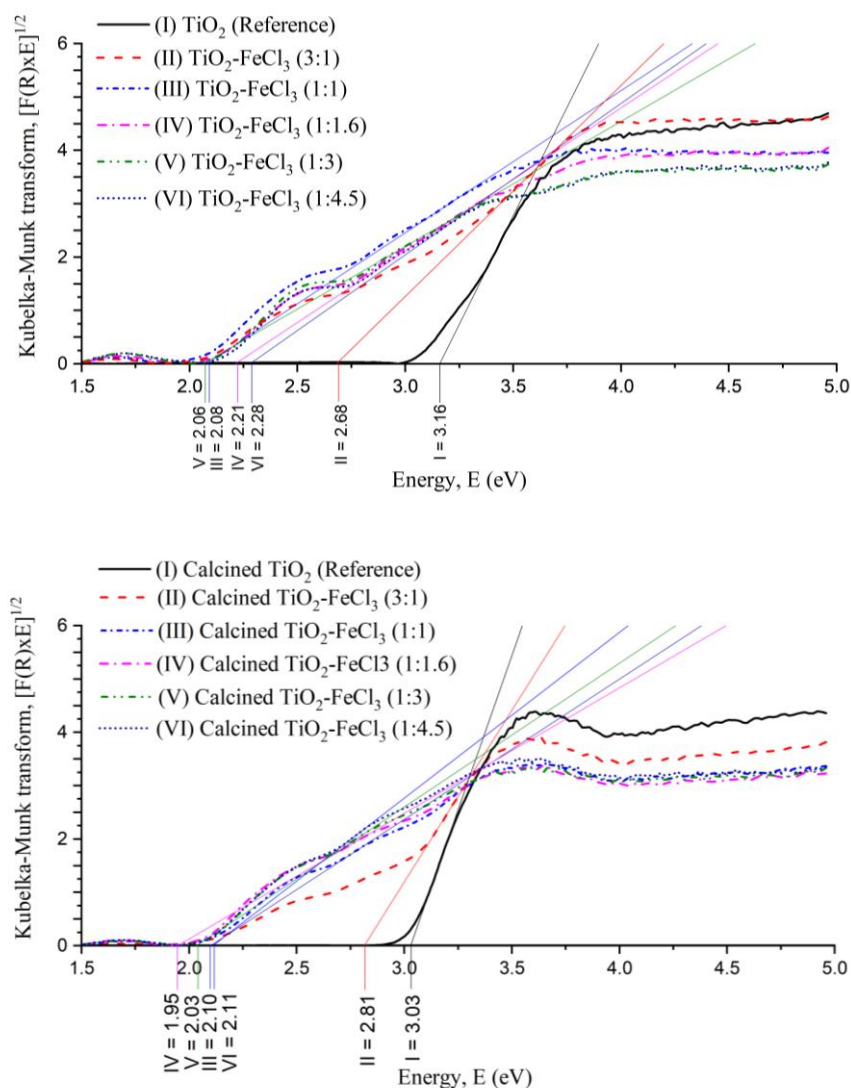


**Figure 5.** Plot of Kubelka–Munk transform versus the Energy of the light absorbed for the undoped  $\text{TiO}_2$  (reference) and the samples synthesized before calcination (**top**) and after calcination (**bottom**).

Therefore, the incorporation of  $\text{Fe}^{3+}$  into the  $\text{TiO}_2$  lattice causes a decrease in the energy band gaps. This effect is observed comparing the reference  $\text{TiO}_2$  with the  $\text{TiO}_2\text{-FeCl}_3$  ratio (1:1). Its band gap energy decreases from 3.16 eV to 2.08 eV.

### 2.5. Evaluation of the Photocatalytic Activity of the Doped Material

Figure 6 presents the results of photocatalytic efficiency before and after the calcination process. After 3 h of irradiation, the samples after calcination showed a photocatalytic efficiency of less than 70%, except for the calcined  $\text{TiO}_2$  (74.0%). Regarding the samples synthesized after the calcination process, the different ratios of  $\text{TiO}_2\text{:FeCl}_3$  (3:1), (1:1.1), (1:1.16), (1:3), and (1:4.5) showed lower photocatalytic efficiency, i.e., 31.1%, 36.7%, 45.5%, 36.3%, 32.6%, respectively. In contrast, all the samples synthesized before the calcination process show a photocatalytic efficiency higher than 70%. The synthesized sample with the best photocatalytic efficiency was  $\text{TiO}_2\text{:FeCl}_3$  (1:16), with a percentage of 93.8%. The reference  $\text{TiO}_2$  showed a similar photocatalytic efficiency, i.e., 92.43%. The remain-

ing samples,  $\text{TiO}_2:\text{FeCl}_3$  (3:1), (1:1), (1:3), and (1:4.5), showed 88.7%, 83.2%, 74.5%, and 83.6%, respectively.

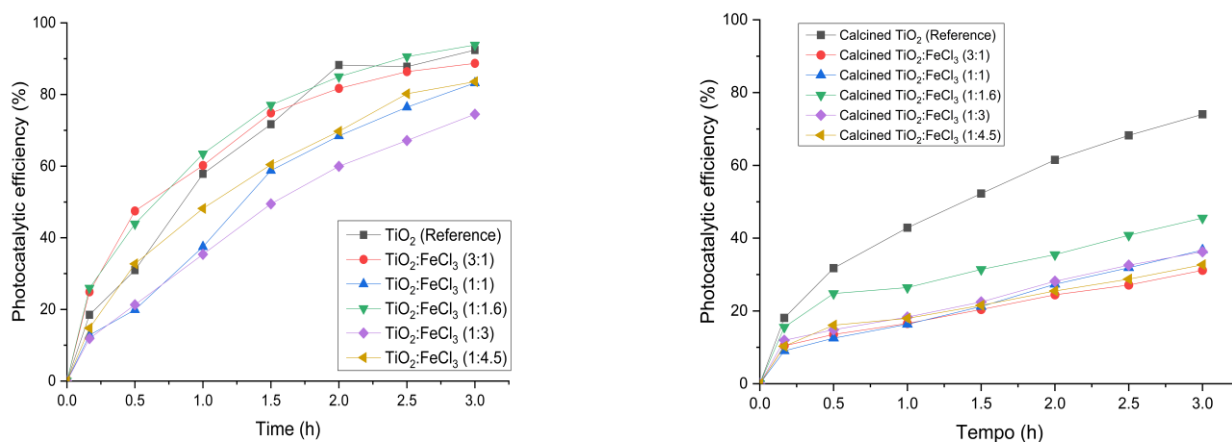


**Figure 6.** Photocatalytic efficiency for  $\text{TiO}_2$  (reference), calcined  $\text{TiO}_2$ , and the synthesized samples before calcination (left) and after calcination (right).

The subsequent use of photocatalysts to determine photocatalytic efficiency is a performance measure. For this purpose, the  $\text{TiO}_2:\text{FeCl}_3$  (1:1.16), as a better catalyst, and the  $\text{TiO}_2$  (reference) samples were submitted to four recycling cycles. As shown in Figure 7, the RhB degradation occurred in all cycles, indicating that both samples were still active during the final cycle. About 10%, 15%, and 20% of the photocatalyst were lost during the filtration and cleaning processes after cycles 1, 2, and 3, respectively. Thus, the loss of the photocatalyst may have contributed to the degradation rate decrease, from 93.8% to 88.1% and from 92.4% to 87.3% for  $\text{TiO}_2:\text{FeCl}_3$  (1:1.16) and  $\text{TiO}_2$  (reference), respectively.

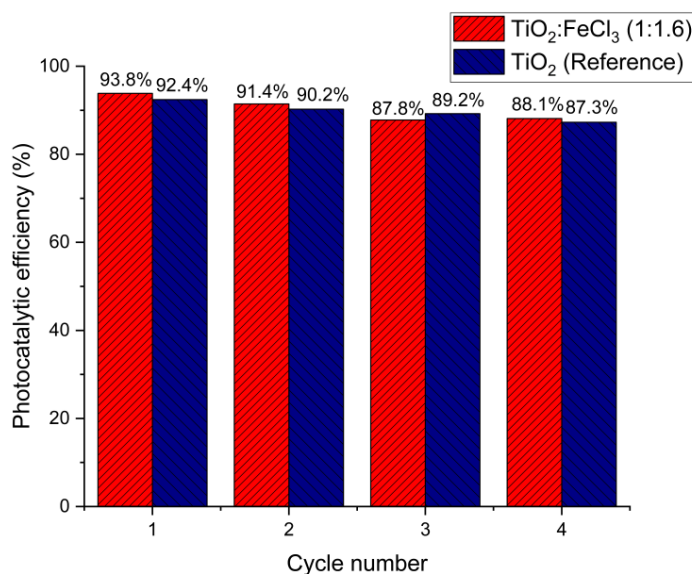


**Figure 7.** Recycling of  $\text{TiO}_2:\text{FeCl}_3$  (1:1.6) and  $\text{TiO}_2$  (reference) for degradation of RhB dye.

Through XRD it was observed that there is an ART after the calcination process, which may influence the photocatalytic efficiency. In SEM analyses, a decrease in the surface area was observed, which also influences the photocatalytic efficiency. According to Kim et al. (2014), this occurs because the diffusion radius of the  $\bullet\text{OH}$  radical is generated in the anatase phase and not in the rutile phase. Consequently, photocatalytic oxidation in the rutile phase is restricted since the reaction zone of the  $\bullet\text{OH}$  radical is restricted to

the surface in the rutile phase, and in the anatase phase, the diffusion radius of the  $\bullet\text{OH}$  radical is larger. Thus, the anatase phase has a higher photocatalytic activity than the rutile phase [39].

Although some samples showed similar photocatalytic efficiency during the 3 h period, their absorption spectra are presented in Figure 8. In fact, the  $\text{TiO}_2$  (reference) and doped  $\text{TiO}_2\text{-FeCl}_3$  (1:1.16) ratio material showed a photocatalytic efficiency of 92.4% and 93.8%, respectively. Through the absorption curves, it can be seen that the RhB molecules are likely to have undergone a more advanced degradation process for the  $\text{TiO}_2\text{-FeCl}_3$  (1:1.16) sample than for  $\text{TiO}_2$  (reference). Thus, it can be concluded that at the ratio (1:1.16), a higher and better photocatalytic efficiency occurs.

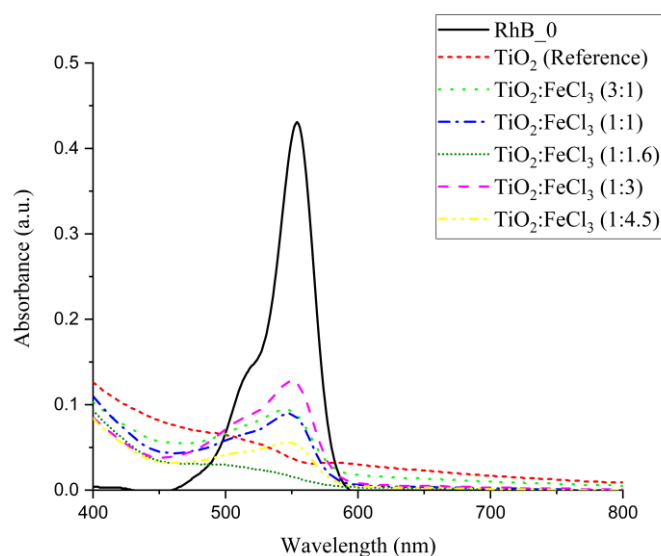


**Figure 8.** Absorbance degradation curves of RhB solution after 3 h of exposure to solar irradiation for the different ratios of doped  $\text{TiO}_2\text{:FeCl}_3$  and  $\text{TiO}_2$  (reference). Where RhB\_0 is the RhB solution (2 ppm) at time 0 not irradiated.

### 3. Materials and Methods

The materials used were  $\text{TiO}_2$  semiconductor nanoparticles (Aeroxide  $\text{TiO}_2$  P25) purchased from Quimidroga (Barcelona, Spain), and their main properties were a purity >99.5%. The Iron (III) chloride ( $\text{FeCl}_3$ ) and Rhodamine B were purchased from Sigma-Aldrich (Lisboa, Portugal). Distilled water was used as a solvent.

An iron ( $\text{Fe}^{3+}$ ) doping process was carried out using semiconductor nanoparticles. First, solutions containing a suspension of  $\text{TiO}_2$  in distilled water (0.01 g/L) were prepared, and aqueous solutions containing different concentrations of  $\text{FeCl}_3$  were based on the concentration of  $\text{TiO}_2$ . Subsequently, both solutions were mixed and stirred at 70 °C for 150 min, and then they were filtered and washed with distilled water. Finally, the samples were dried at 60 °C to obtain a solid material [10].

The  $\text{TiO}_2\text{:FeCl}_3$  concentrations selected to reach the lowest band gap energy reduction were (3:1), (1:1), (1:1.6), (1:3), and (1:4.5). For example, the ratio (1:3) means that the sample was made with a concentration of 0.01 g/mL of  $\text{TiO}_2$  and 0.03 g/mL of  $\text{FeCl}_3$ . The particle identification ( $\text{TiO}_2\text{:FeCl}_3$ ) was added to their concentration ratio to identify the testing samples. Subsequently, the powders (doped and undoped  $\text{TiO}_2$  nanoparticles) were subjected to a calcination process (3 h at 700 °C) [6].

The band gap of the semiconductor nanoparticles was initially analyzed using diffuse reflectance spectroscopy (DRS) and Kubelka–Munk transform to study the effectiveness of doping and calcination. Subsequently, x-ray diffraction (XRD) was used to identify the crystalline phase of each material, as well as lattice parameters, crystal cell volume, and anatase phase fraction. Fourier transform infrared spectroscopy (FTIR) was performed to

analyze the chemical composition of the doped materials. Scanning electron microscopy (SEM) was performed to analyze the homogenization and particle size of the samples. Energy dispersive spectroscopy (EDS) was performed to obtain the chemical composition of the doped materials. The doped semiconductor nanoparticles were subsequently immersed in RhB solution to analyze the photocatalytic activity under a sunlight simulator.

### 3.1. Diffuse Reflectance Spectroscopy (DRS) and Kubelka–Munk Transform

In the first stage, to determine the band gap energy of the reference concentration of TiO<sub>2</sub> (undoped) and the various concentrations of doped TiO<sub>2</sub>-FeCl<sub>3</sub> before and after the calcination process, Ultraviolet-Visible diffuse reflectance spectroscopy absorption measurements were performed. This analytical method is similar to the usual UV-vis spectroscopy, except that it is reflected into an integrating sphere and collected instead of transmitting light. Parallel to transmittance for liquids, reflectance, R, is advantageous for quantifying the amount of light reflected on solid surfaces.

The parameter called Kubelka–Munk function, F(R), was established to determine the light absorption [40]. Afterward, using the Kubelka–Munk transform, it was possible to calculate the band gap energy (E<sub>g</sub>) [41,42].

### 3.2. X-ray Diffraction (XRD)

XRD was used to determine the crystallite phase of TiO<sub>2</sub>-doped materials using x-ray diffraction with a CuK $\alpha$  source from a Philips PW 1710 X-ray diffractometer (Billerica, MA, USA).

The Debye–Scherrer equation was employed to calculate the crystallite size of the doped particles before and after the calcination process [43]. The value of the lattice spacing for each of the selected peaks in the XRD spectrum was estimated from Bragg's law [5]. To determine the fraction of the anatase phase in TiO<sub>2</sub> doped powders, the intensity of the first and most intense XRD peaks of each sample containing the mixture of the two phases were used according to [44].

### 3.3. Fourier-Transform Infrared Spectroscopy (FTIR)

To check the chemical composition of the doped materials, i.e., to identify the chemical bonds existing in the doping of TiO<sub>2</sub> with FeCl<sub>3</sub> in the spectral range from 400 cm<sup>-1</sup> to 4000 cm<sup>-1</sup>, Shimadzu IR-Prestige-21 spectrometer (Kyoto, Japan) was used. The most relevant elements, the chemical bonds in undoped TiO<sub>2</sub> (reference) and different concentrations of TiO<sub>2</sub>-FeCl<sub>3</sub> after the calcination process, were pointed out.

### 3.4. Scanning Electron Microscopy (SEM) and Energy Dispersive Spectroscopy (EDS)

Scanning electron microscopy (SEM) (Houston, TX, USA) was used to analyze the homogenization and dispersion of the doped materials. Energy dispersive spectroscopy (EDS) (Austin, TX, USA) was used to verify their chemical characterization, i.e., what chemical elements and their concentrations in the sample. These analyzes had the main objective of ascertaining the incorporation of FeCl<sub>3</sub> in TiO<sub>2</sub> nanoparticles in the doping process.

### 3.5. Photocatalytic Activity

The photocatalytic efficiency of the doped material was analyzed by Rhodamine B (RhB) degradation. First, 50 mg of nanoparticles were immersed in 50 mL of 2 ppm aqueous RhB solution, and then they were placed in a box 25 cm below a sunlight simulation lamp with a power intensity of 11 W/m<sup>2</sup>. The samples were conditioned in the dark for 80 min and then exposed to light for 3 h. Therefore, the initial adsorption and photocatalysis were split, and this phenomenon could be accurately analyzed. To prevent evaporation of the RhB solution, the systems were covered with a transparent cling film with less than 10% absorbance and reflectance (between 292 and 900 nm), allowing the almost total light transmission to the samples [45]. The photocatalytic degradation of the RhB solutions was monitored through their maximum absorbance values obtained at

different time intervals [5,46,47]. During the test, aliquots of 5 mL were withdrawn from the systems and then centrifuged at 6000 rpm for 30 min to obtain decantation of the doped material. Subsequently, aliquots of 5 mL were taken from the centrifuged dispersions, and their absorbance was then measured using a spectrophotometer (SanSpecUV-Vis) in a wavelength range of 400 to 800 nm. The samples' photocatalytic efficiency was calculated over time to assess their performance and select the best concentration of TiO<sub>2</sub>-FeCl<sub>3</sub> regarding photodegradation.

To calculate the photocatalytic efficiency, the maximum absorbance (554 nm) of the dye (RhB) was monitored as a function of time (using a Shimadzu 3101 PC) and determined according to [48]. The best samples considering the photocatalytic efficiency will be submitted to four cycling experiments at the same conditions as the initial tests in order to analyze the stability of the prepared photocatalysts.

#### 4. Conclusions

The main objective of this research was to assess doped TiO<sub>2</sub> semiconductor nanoparticles with different contents of FeCl<sub>3</sub>, before and after calcination, through their optical, structural, morphological, chemical, and photocatalytic properties. The following conclusions can be drawn from the results obtained:

- The process of doping TiO<sub>2</sub> with FeCl<sub>3</sub> provided changes in the optical properties of the material and a decrease in the E<sub>g</sub> of TiO<sub>2</sub>, also after the calcination process. The doping concentrations that presented the lowest E<sub>g</sub> values were (1:1), (1:1.6), and (1:3).
- Contrarily to the effect after calcination, in the doping process the nanoparticles have no significant influence on the anatase-to-rutile transformation (ART) compared to the reference TiO<sub>2</sub>.
- The Fe-doping process modified the reference TiO<sub>2</sub> spectrum with higher intensity of hydroxyl bonds and vibration of the Ti–O–Fe bond. After the calcination process, a drastic reduction of these bonds occurred.
- The particles are within the nanometer scale, and there are indications of the chemical reaction between TiO<sub>2</sub> and Fe. The calcination process causes a relevant increase in particle size and surface smoothing.
- The ratio (1:1.6) of TiO<sub>2</sub>:FeCl<sub>3</sub> showed the highest activity in the photocatalytic degradation of RhB with an efficiency of 93.8% after 3 h of irradiation.

In conclusion: doping TiO<sub>2</sub> nanoparticles using metal ions (e.g., Fe<sup>3+</sup>) will improve photocatalytic activity under visible light irradiation, becoming a promising material for low-cost photocatalytic processes. However, further investigations for industrial-scale applications are needed to characterize the material's durability in photocatalytic processes. The doped TiO<sub>2</sub> will be applied in different materials for self-cleaning processes, for air purification, e.g., in polymeric materials, ceramics, textiles, and also in civil engineering (e.g., in cementitious materials and asphalt mixtures).

**Author Contributions:** Conceptualization, C.A., O.L.J. and I.R.S.; methodology, I.R.S., S.L.J., E.F., M.P. and J.C.; validation, I.R.S., S.L.J. and M.P.; formal analysis, C.A., O.L.J., N.H. and I.R.S.; investigation, C.A., I.R.S., S.L.J. and J.C.; resources, J.C., M.F.M.C. and E.F.; data curation, S.L.J. and I.R.S.; writing—original draft preparation, C.A., O.L.J., I.R.S. and S.L.J.; writing—review and editing, É.M., N.H., E.F., M.F.M.C. and J.C.; visualization, I.R.S., S.L.J. and O.L.J.; supervision, I.R.S., E.F. and J.C.; project administration, E.F. and J.C.; funding acquisition, E.F., M.F.M.C. and J.C. All authors have read and agreed to the published version of the manuscript.

**Funding:** This research was partially funded by the Portuguese Foundation for Science and Technology (FCT), NanoAir PTDC/FISMAC/6606/2020, MicroCoolPav EXPL/EQU-EQU/1110/2021, UIDB/04650/2020, and UIDB/04029/2020. This research was supported by the doctoral Grant PRT/BD/154269/2022 financed by Portuguese Foundation for Science and Technology (FCT), and with funds from POR Norte - Portugal 2020 and State Budget, under MIT Portugal Program. The third author would like to acknowledge the FCT for funding (2022.00763.CEECIND).

**Data Availability Statement:** Not applicable.

**Conflicts of Interest:** The authors declare no conflict of interest.

## References

1. Rocha Segundo, I.; Freitas, E.; Branco, V.T.F.C.; Landi, S.; Costa, M.F.; Carneiro, J.O. Review and analysis of advances in functionalized, smart, and multifunctional asphalt mixtures. *Renew. Sustain. Energy Rev.* **2021**, *151*, 111552. [[CrossRef](#)]
2. Zabihi-Mobarakeh, H.; Nezamzadeh-Ejhieh, A. Application of supported TiO<sub>2</sub> onto Iranian clinoptilolite nanoparticles in the photodegradation of mixture of aniline and 2,4-dinitroaniline aqueous solution. *J. Ind. Eng. Chem.* **2015**, *26*, 315–321. [[CrossRef](#)]
3. Nezamzadeh-Ejhieh, A.; Bahrami, M. Investigation of the photocatalytic activity of supported ZnO–TiO<sub>2</sub> on clinoptilolite nano-particles towards photodegradation of wastewater-contained phenol. *Desalin. Water Treat.* **2015**, *55*, 1096–1104. [[CrossRef](#)]
4. Rocha Segundo, I.; Freitas, E.; Landi, S., Jr.; Costa, M.F.M.; Carneiro, J.O. Smart, Photocatalytic and Self-Cleaning Asphalt Mixtures: A Literature Review. *Coatings* **2019**, *9*, 696. [[CrossRef](#)]
5. Carneiro, J.O.; Azevedo, S.; Fernandes, F.; Freitas, E.; Pereira, M.; Tavares, C.J.; Lanceros-Méndez, S.; Teixeira, V. Synthesis of iron-doped TiO<sub>2</sub> nanoparticles by ball-milling process: The influence of process parameters on the structural, optical, magnetic, and photocatalytic properties. *J. Mater. Sci.* **2014**, *49*, 7476–7488. [[CrossRef](#)]
6. Ghorbanpour, M.; Feizi, A. Iron-doped TiO<sub>2</sub> Catalysts with Photocatalytic Activity. *J. Water Environ. Nanotechnol.* **2019**, *4*, 60–66. [[CrossRef](#)]
7. Zahabizadeh, B.; Segundo, I.R.; Pereira, J.; Freitas, E.; Camões, A.; Tavares, C.J.; Teixeira, V.; Cunha, V.M.C.F.; Costa, M.F.M.; Carneiro, J.O. Development of Photocatalytic 3D-Printed Cementitious Mortars: Influence of the Curing, Spraying Time Gaps and TiO<sub>2</sub> Coating Rates. *Buildings* **2021**, *11*, 381. [[CrossRef](#)]
8. Adamek, E.; Baran, W.; Ziemiańska, Justyna Makowski, A.; Sobczak, A. Use of a TiO<sub>2</sub>/FeCl<sub>3</sub> mixture in environmental cleaning technology. *Proc. ECOpole* **2012**, *6*. [[CrossRef](#)]
9. Wang, J.; Wang, Z.; Zhao, D.; Liang, Y.; Wang, H.; Wang, N.; Jiang, W.; Liu, S.; Liu, C.; Ding, W.; et al. Preparation, structural and photocatalytic activity of Sn/Fe co-doped TiO<sub>2</sub> nanoparticles by sol-gel method. *Ceram. Int.* **2022**, *48*, 8297–8305. [[CrossRef](#)]
10. Lucas, S.S.; Ferreira, V.M.; de Aguiar, J.L.B. Incorporation of titanium dioxide nanoparticles in mortars—Influence of microstructure in the hardened state properties and photocatalytic activity. *Cem. Concr. Res.* **2013**, *43*, 112–120. [[CrossRef](#)]
11. Di Valentin, C.; Finazzi, E.; Pacchioni, G.; Selloni, A.; Livraghi, S.; Paganini, M.C.; Giamello, E. N-doped TiO<sub>2</sub>: Theory and experiment. *Chem. Phys.* **2007**, *339*, 44–56. [[CrossRef](#)]
12. Alkorbi, A.S.; Muhammad Asif Javed, H.; Hussain, S.; Latif, S.; Mahr, M.S.; Mustafa, M.S.; Alsaiari, R.; Alhemiary, N.A. Solar light-driven photocatalytic degradation of methyl blue by carbon-doped TiO<sub>2</sub> nanoparticles. *Opt. Mater.* **2022**, *127*, 112259. [[CrossRef](#)]
13. Barakat, M.A.; Schaeffer, H.; Hayes, G.; Ismat-Shah, S. Photocatalytic degradation of 2-chlorophenol by Co-doped TiO<sub>2</sub> nanoparticles. *Appl. Catal. B Environ.* **2005**, *57*, 23–30. [[CrossRef](#)]
14. Cao, X.; Yang, X.; Li, H.; Huang, W.; Liu, X. Investigation of Ce-TiO<sub>2</sub> photocatalyst and its application in asphalt-based specimens for NO degradation. *Constr. Build. Mater.* **2017**, *148*, 824–832. [[CrossRef](#)]
15. Etacheri, V.; Di Valentin, C.; Schneider, J.; Bahnemann, D.; Pillai, S.C. Visible-light activation of TiO<sub>2</sub> photocatalysts: Advances in theory and experiments. *J. Photochem. Photobiol. C Photochem. Rev.* **2015**, *25*, 1–29. [[CrossRef](#)]
16. Eadi, S.B.; Kim, S.; Jeong, S.W.; Jeon, H.W. Novel Preparation of Fe Doped TiO<sub>2</sub> Nanoparticles and Their Application for Gas Sensor and Photocatalytic Degradation. *Adv. Mater. Sci. Eng.* **2017**, *2017*, 2191659. [[CrossRef](#)]
17. Zaleska, A. Doped-TiO<sub>2</sub>: A Review. *Recent Patents Eng.* **2008**, *2*, 157–164. [[CrossRef](#)]
18. Ganesh, I.; Kumar, P.; Gupta, A.; Sekhar, P.; Radha, K.; Padmanabham, G.; Sundararajan, G. Preparation and characterization of Fe-doped TiO<sub>2</sub> powders for solar light response and photocatalytic applications. *Process. Appl. Ceram.* **2012**, *6*, 21–36. [[CrossRef](#)]
19. Piątkowska, A.; Janus, M.; Szymański, K.; Mozia, S. C-,N- and S-Doped TiO<sub>2</sub> Photocatalysts: A Review. *Catalysts* **2021**, *11*, 144. [[CrossRef](#)]
20. Landi, S.; Carneiro, J.; Soares, O.S.G.P.; Pereira, M.F.R.; Gomes, A.C.; Ribeiro, A.; Fonseca, A.M.; Parpot, P.; Neves, I.C. Photocatalytic performance of N-doped TiO<sub>2</sub>/nano-SiO<sub>2</sub>-HY nanocomposites immobilized over cotton fabrics. *J. Mater. Res. Technol.* **2019**, *8*, 1933–1943. [[CrossRef](#)]
21. Liu, C.; Mao, S.; Shi, M.; Wang, F.; Xia, M.; Chen, Q.; Ju, X. Peroxymonosulfate activation through 2D/2D Z-scheme CoAl-LDH/BiOBr photocatalyst under visible light for ciprofloxacin degradation. *J. Hazard. Mater.* **2021**, *420*, 126613. [[CrossRef](#)] [[PubMed](#)]
22. Liu, C.; Mao, S.; Shi, M.; Hong, X.; Wang, D.; Wang, F.; Xia, M.; Chen, Q. Enhanced photocatalytic degradation performance of BiVO<sub>4</sub>/BiOBr through combining Fermi level alteration and oxygen defect engineering. *Chem. Eng. J.* **2022**, *449*, 137757. [[CrossRef](#)]
23. Venturini, L.; Bacchi, I. Research, Design and Development of a Photocatalytic Asphalt Pavement. In Proceedings of the 2nd International Conference on Environmentally Friendly Roads, ENVIROAD 2009, Warsaw, Poland, 15–16 October 2009; pp. 1–16.
24. Cano-Casanova, L.; Ansón-Casaos, A.; Hernández-Ferrer, J.; Benito, A.M.; Maser, W.K.; Garro, N.; Lillo-Ródenas, M.A.; Román-Martínez, M.C. Surface-Enriched Boron-Doped TiO<sub>2</sub> Nanoparticles as Photocatalysts for Propene Oxidation. *ACS Appl. Nano Mater.* **2022**, *5*, 12527–12539. [[CrossRef](#)] [[PubMed](#)]

25. Cano-Casanova, L.; Amorós-Pérez, A.; Ouzzine, M.; Lillo-Ródenas, M.A.; Román-Martínez, M.C. One step hydrothermal synthesis of TiO<sub>2</sub> with variable HCl concentration: Detailed characterization and photocatalytic activity in propene oxidation. *Appl. Catal. B Environ.* **2018**, *220*, 645–653. [[CrossRef](#)]
26. Qin, Q.; Wang, J.; Xia, Y.; Yang, D.; Zhou, Q.; Zhu, X.; Feng, W. Synthesis and Characterization of Sn/Ni Single Doped and Co-Doped Anatase/Rutile Mixed-Crystal Nanomaterials and Their Photocatalytic Performance under UV-Visible Light. *Catalysts* **2021**, *11*, 1341. [[CrossRef](#)]
27. Fan, W.; Chan, K.Y.; Zhang, C.; Zhang, K.; Ning, Z.; Leung, M.K.H. Solar photocatalytic asphalt for removal of vehicular NO<sub>x</sub>: A feasibility study. *Appl. Energy* **2018**, *225*, 535–541. [[CrossRef](#)]
28. Tang, B.; Liu, X.; Huang, W.; Cao, X. Preparation of La-doped nanometer TiO<sub>2</sub> and its application for NO removal on asphalt concrete. *Road Mater. Pavement Des.* **2017**, *18*, 43–53. [[CrossRef](#)]
29. Yeganeh, M.; Shahtahmasebi, N.; Kompany, A.; Karimipour, M.; Razavi, F.; Nasralla, N.H.S.; Šiller, L. The magnetic characterization of Fe doped TiO<sub>2</sub> semiconducting oxide nanoparticles synthesized by sol-gel method. *Phys. B Condens. Matter* **2017**, *511*, 89–98. [[CrossRef](#)]
30. Ali, T.; Tripathi, P.; Azam, A.; Raza, W.; Ahmed, A.S.; Ahmed, A.; Muneer, M. Photocatalytic performance of Fe-doped TiO<sub>2</sub> nanoparticles under visible-light irradiation. *Mater. Res. Express* **2017**, *4*, 015022. [[CrossRef](#)]
31. Sood, S.; Umar, A.; Mehta, S.K.; Kansal, S.K. Highly effective Fe-doped TiO<sub>2</sub> nanoparticles photocatalysts for visible-light driven photocatalytic degradation of toxic organic compounds. *J. Colloid Interface Sci.* **2015**, *450*, 213–223. [[CrossRef](#)]
32. Xiang, L.; Zhao, X. Wet-Chemical Preparation of TiO<sub>2</sub>-Based Composites with Different Morphologies and Photocatalytic Properties. *Nanomaterials* **2017**, *7*, 310. [[CrossRef](#)] [[PubMed](#)]
33. Kutuzova, A.; Dontsova, T. Synthesis, characterization and properties of titanium dioxide obtained by hydrolytic method. In Proceedings of the 2017 IEEE 7th International Conference Nanomaterials: Application & Properties (NAP), Odessa, Ukraine, 10–15 September 2017; IEEE: Hoboken, NJ, USA, 2017; pp. 01NNPT02-1–01NNPT02-5.
34. Homem, N.C.; Yamaguchi, N.U.; Vieira, M.F.; Amorim, M.T.S.P.; Bergamasco, R. Surface modification of microfiltration membrane with GO nanosheets for dyes removal from aqueous solutions. *Chem. Eng. Trans.* **2017**, *60*, 259–264. [[CrossRef](#)]
35. Ribao, P.; Corredor, J.; Rivero, M.J.; Ortiz, I. Role of reactive oxygen species on the activity of noble metal-doped TiO<sub>2</sub> photocatalysts. *J. Hazard. Mater.* **2019**, *372*, 45–51. [[CrossRef](#)] [[PubMed](#)]
36. Shahmoradi, B.; Maleki, A.; Byrappa, K. Removal of Disperse Orange 25 using in situ surface-modified iron-doped TiO<sub>2</sub> nanoparticles. *Desalin. Water Treat.* **2015**, *53*, 3615–3622. [[CrossRef](#)]
37. Marami, M.B.; Farahmandjou, M.; Khoshnevisan, B. Sol-Gel Synthesis of Fe-Doped TiO<sub>2</sub> Nanocrystals. *J. Electron. Mater.* **2018**, *47*, 3741–3748. [[CrossRef](#)]
38. Tonejc, A.; Djerdj, I.; Tonejc, A. An analysis of evolution of grain size-lattice parameters dependence in nanocrystalline TiO<sub>2</sub> anatase. *Mater. Sci. Eng. C* **2002**, *19*, 85–89. [[CrossRef](#)]
39. Kim, W.; Tachikawa, T.; Moon, G.; Majima, T.; Choi, W. Molecular-Level Understanding of the Photocatalytic Activity Difference between Anatase and Rutile Nanoparticles. *Angew. Chemie Int. Ed.* **2014**, *53*, 14036–14041. [[CrossRef](#)]
40. Valencia, S.; Marin, J.M.; Restrepo, G. Study of the Bandgap of Synthesized Titanium Dioxide Nanoparticles Using the Sol-Gel Method and a Hydrothermal Treatment. *Open Mater. Sci. J.* **2010**, *4*, 9–14. [[CrossRef](#)]
41. Landi, S.; Segundo, I.R.; Freitas, E.; Vasilevskiy, M.; Carneiro, J.; Tavares, C.J. Use and misuse of the Kubelka-Munk function to obtain the band gap energy from diffuse reflectance measurements. *Solid State Commun.* **2022**, *341*, 114573. [[CrossRef](#)]
42. Landi, S.; Segundo, I.R.; Afonso, C.; Lima, O.; Costa, M.F.M.; Freitas, E.; Carneiro, J. Evaluation of band gap energy of TiO<sub>2</sub> precipitated from titanium sulphate. *Phys. B Condens. Matter* **2022**, *639*, 414008. [[CrossRef](#)]
43. Jenkins, R.; Snyder, R. *Introduction to X-ray Powder Diffractometry*; Wiley-Interscience: New York, NY, USA, 1996; ISBN 978-0-471-51339-1.
44. Spurr, R.A.; Myers, H. Quantitative Analysis of Anatase-Rutile Mixtures with an X-Ray Diffractometer. *Anal. Chem.* **1957**, *29*, 760–762. [[CrossRef](#)]
45. Rocha Segundo, I.; Ferreira, C.; Freitas, E.F.; Carneiro, J.O.; Fernandes, F.; Júnior, S.L.; Costa, M.F.; Landi Júnior, S.; Costa, M.F. Assessment of photocatalytic, superhydrophobic and self-cleaning properties on hot mix asphalts coated with TiO<sub>2</sub> and/or ZnO aqueous solutions. *Constr. Build. Mater.* **2018**, *166*, 36–44. [[CrossRef](#)]
46. Yang, X.; Cao, C.; Erickson, L.; Hohn, K.; Maghirang, R.; Klabunde, K. Photo-catalytic degradation of Rhodamine B on C-, S-, N-, and Fe-doped TiO<sub>2</sub> under visible-light irradiation. *Appl. Catal. B Environ.* **2009**, *91*, 657–662. [[CrossRef](#)]
47. Barkhade, T.; Banerjee, I. Photocatalytic degradation of Rhodamine B dye using Fe doped TiO<sub>2</sub> nanocomposites. *AIP Conf. Proc.* **2018**, *1961*, 030016.
48. Carneiro, J.O.; Azevedo, S.; Teixeira, V.; Fernandes, F.; Freitas, E.; Silva, H.; Oliveira, J. Development of photocatalytic asphalt mixtures by the deposition and volumetric incorporation of TiO<sub>2</sub> nanoparticles. *Constr. Build. Mater.* **2013**, *38*, 594–601. [[CrossRef](#)]

**Disclaimer/Publisher’s Note:** The statements, opinions and data contained in all publications are solely those of the individual author(s) and contributor(s) and not of MDPI and/or the editor(s). MDPI and/or the editor(s) disclaim responsibility for any injury to people or property resulting from any ideas, methods, instructions or products referred to in the content.